HIGH RESOLUTION COMPUTED TOMOGRAPHY FOR MODELLING LAMINATE DAMAGE

P. Wright, A.J. Moffat, A. Renault, I. Sinclair, S.M. Spearing
School of Engineering Sciences, University of Southampton, SO17 1BJ, U.K.
Pete.Wright@soton.ac.uk

SUMMARY

In situ synchrotron radiation computed tomography has been used during tensile testing of CFRP $[90/0]_S$ laminates to obtain 3D images of initiation and propagation of sub-critical damage. The damage has been quantified to provide detailed initialisation and validation of 3D finite element modelling of splitting in 0º plies and transverse ply cracks.

Keywords: Synchrotron X-ray, computed tomography, 3D damage model, matrix cracking

INTRODUCTION

Sub-critical damage in laminated carbon fibre-epoxy composites under tension consists primarily of matrix cracks, inter-ply delaminations and fibre fracture [1, 2]. There are many models that attempt to predict the strength of laminated composites in terms of damage propagation [3-5], however few of these models are based on a full description of micromechanics of these sub-critical damage mechanisms. Previous studies [6] have demonstrated the 3D nature of multiple interacting damage mechanisms, though the extent to which the mechanisms and the material microstructure (*e.g.* resin rich regions and toughening precipitates) should be modelled to obtain accurate predictions of failure is not apparent. One of the restricting factors for accurate model predictions may lie with the lack of readily available experimental data providing quantitative microstructure-level observations of damage progression, from initial onset of matrix cracking to delamination and final failure. Numerous techniques have been applied to investigate damage in laminated composites, including ultrasound, electron microscopy and acoustic emission spectroscopy [7-10]. Each of these methods however has its limitations, with factors such as sectioning artefacts, limited spatial resolution, post-mortem utilisation *etc.* compromising a complete micromechanical characterisation (spatial and temporal) of internal failure processes.

X-ray computed tomography (CT) is being increasingly utilised for material characterisation [11,12] with the work presented in this paper addressing high resolution synchrotron radiation CT (SRCT) as a non-destructive technique to evaluate in 3D the dominant micromechanisms and interactions involved in sub-critical damage in $[90/0]_S$ laminates loaded in uni-axial tension. The essentially non-destructive, non-contacting nature of CT imaging provides valuable opportunities for *in situ* investigation. In addition to qualitative visualisation of damage morphology, quantitative data for crack opening and shear displacements in 0º ply splits and

transverse ply cracks (TPCs) has been extracted from within the sample bulk. These observations inform the development of FE models of 0º ply splitting and transverse ply cracking, with experimental crack opening data being directly compared with model predictions.

MATERIALS AND EXPERIENTAL METHOD

Double notched tensile samples were produced from laminated panels of Hexcel HexPly® M21 carbon fiber-epoxy pre-preg. The panels were laid up in a $[90/0]_S$ configuration with total laminate thickness of 1 mm (post cure) and cured to the manufacturer's specifications (pressure of 1 bar under vacuum and 7 bar in an autoclave, heat-up at 2°C/min to 180°C, hold at 180ºC for 120 minutes, cooled at 4°C/min to ambient room temperature). Samples were machined using an abrasive waterjet to create double edge notched (DEN) samples as shown in Figure 1. Radiographic analysis prior to loading showed negligible damage occurred due to machining.

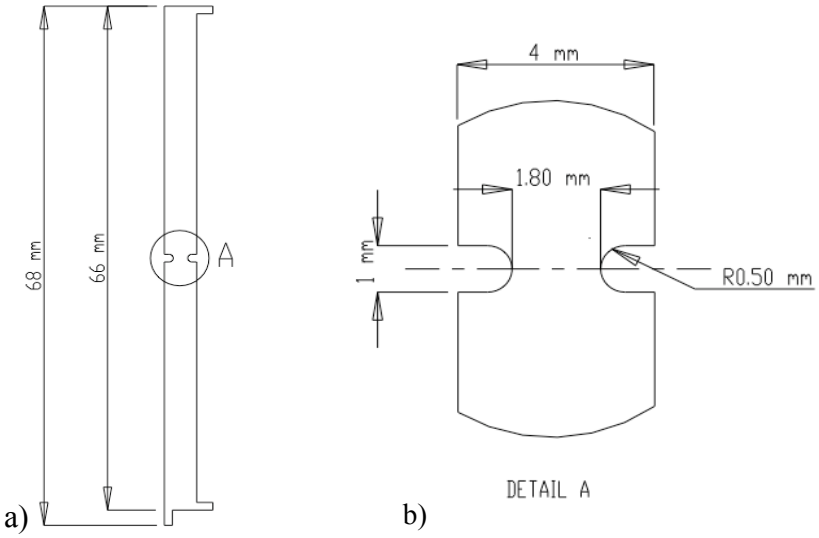

Figure 1: (a) Geometry of laminate samples, and (b) notch detail.

Aluminium tabs were adhesively bonded to the samples for uni-axial tensile loading in a screw driven load frame (Figure 2). The sample was located in the load frame using two restraining fingers to grip the tabs. A load was applied through a screw driven shaft attached to the finger restraints via a pin that eliminated torsion. Loading was monitored via a calibrated load cell. Several samples were tested to failure and a mean failure stress of 960 MPa was recorded.

To obtain CT data a series of 2D radiographs were collected as the sample was rotated relative to a detector. Filtered back projection was used for subsequent volume reconstruction [13]. SRCT imaging took place at the ID19 beamline within the European Synchrotron Radiation Facility (ESRF) in Grenoble, France. This provides a monochromatic and highly coherent source of X-rays that can be exploited for phase contrast (edge detection regime in this experiment) in addition to absorption [14]. A load frame was attached to a precision motorized stage with the sample positioned 37

mm from a 14 bit fast read-out, low noise (FReLoN) detector attached to a 2048 x 2048 pixel CCD camera. An isotropic voxel size of 1.4 μm was achieved for this work. During each tomographic scan 1000 radiographs were collected at regular increments during a 180° rotation. The exposure time for each radiograph was 50 ms, which resulted in scan times of less than 4 minutes. The radiographs were reconstructed using ESRF in-house software and the resulting 3-D volumes were analysed using commercially available software and various routines using Matlab and VTK. To monitor crack evolution, samples were imaged at increasing stresses, from 30-90 % σ_f. Several samples were also loaded to a given stress level and then scanned in the loaded and unloaded state to enable the separation of externally applied and internal thermal residual stress effects.

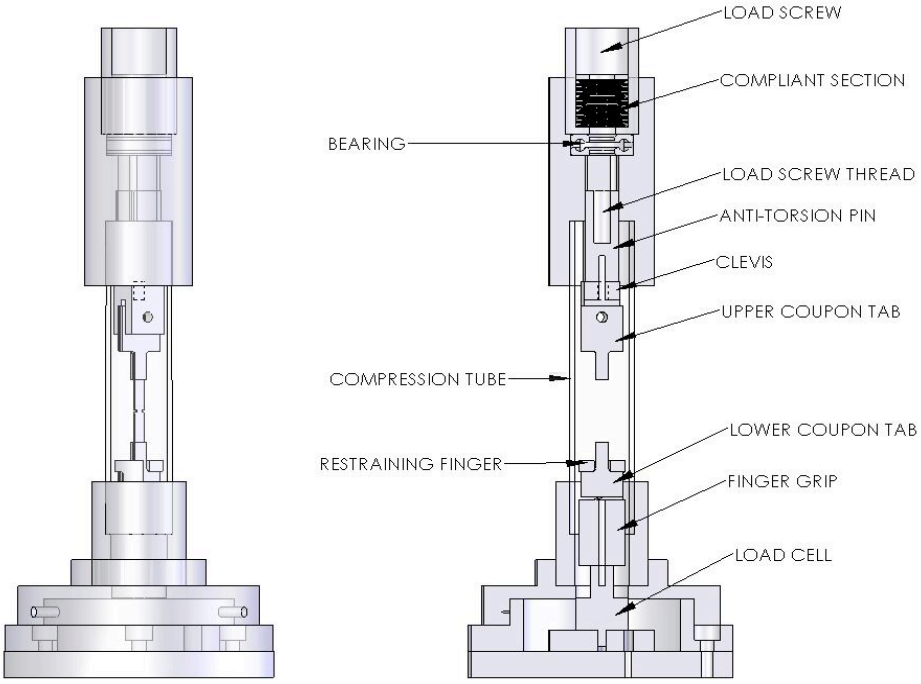

Figure 2: (a) Semi-transparent schematic of *in situ* CT load frame, and (b) annotated cross-section.

RESULTS AND DISCUSSION

Qualitative Observations and Effects of Microstructure

The tomographic volume is represented as a grey-scale map of the material as a function of local X-ray absorption coefficient, along with light/dark fringes at material interfaces (absorption and phase contrast). Figure 3 shows 2D slices of a volume in which matrix cracks in both 0º and 90º plies can be seen, with the cracks being highlighted by fringes at the air/material interface.

The resin used in the material contains rubber particles that have precipitated during the cure cycle: these are identifiable in Figure 3 where particle-matrix decohesion has also been observed. The greatest density of the particles occurs in resin rich regions.

These regions coincide with the pre-preg ply construction, where each ply of 250 µm thickness is composed of two half-thickness plies.

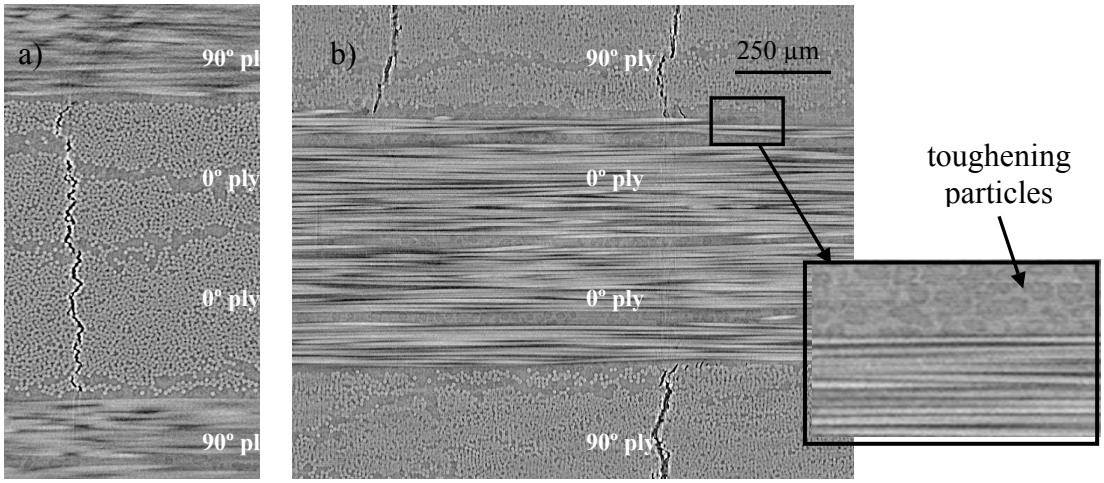

Figure 3: 2D tomographic slice images of: (a) 0º matrix cracking, slice perpendicular to the loading direction, and (b) 90º transverse ply cracking, slice perpendicular to the loading direction.

The cracks in the notched region have been segmented from the undamaged material to show the 3D structure of the damage, with Figure 4 showing the resultant damage state in a sample loaded to 50% σ_f (the undamaged material has been cropped from front part of the volume to reveal two 0º splits at each notch and a TPC). It is observed that the 0º splits do not grow with a flat crack front, rather crack pinning occurs at multiple locations along the front. Analysis of the 3D volume in conjunction with 2D slices at particular positions along the split show that these pinning locations coincide with resin rich regions, indicating that the local microstructure has a large impact on the morphology of the matrix cracks.

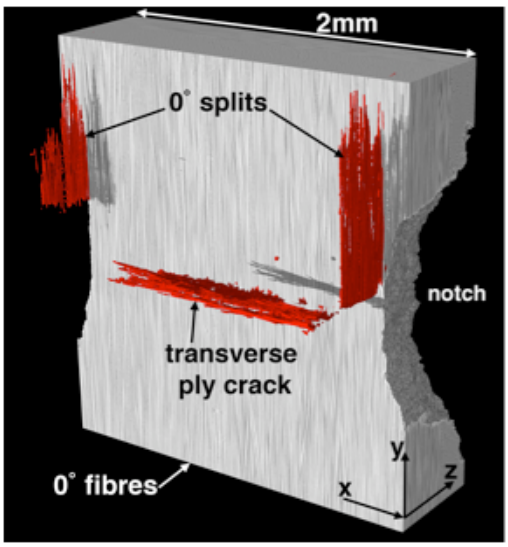

Figure 4: Tomography image of intralaminar damage in a $[90/0]_S$ laminate. The bulk of the composite has been withdrawn to reveal the damage (red).

Quantitative Damage Characterisation

Quantitative data has been extracted from an analysis of the tomography images of the samples at various loads. Crack opening displacement (COD) of the 0º splits and TPCs was calculated directly from individually segmented cracks such as those shown in Figure 4. A routine to calculate the number of voxels (volume elements) across the split opening was implemented. Figure 5 shows a plot of COD as a function of crack length and ply thickness for a 0º ply split and TPC that was created from the voxel data. Regions of crack bridging and pinning can particularly evident in the 0˚ ply crack in Figure 5(a); whilst the TPC crack shape is Figure 5(b) is strongly defined by the 0˚/90˚ ply interface, microstructural irregularities are evident in both the crack shape and opening levels.

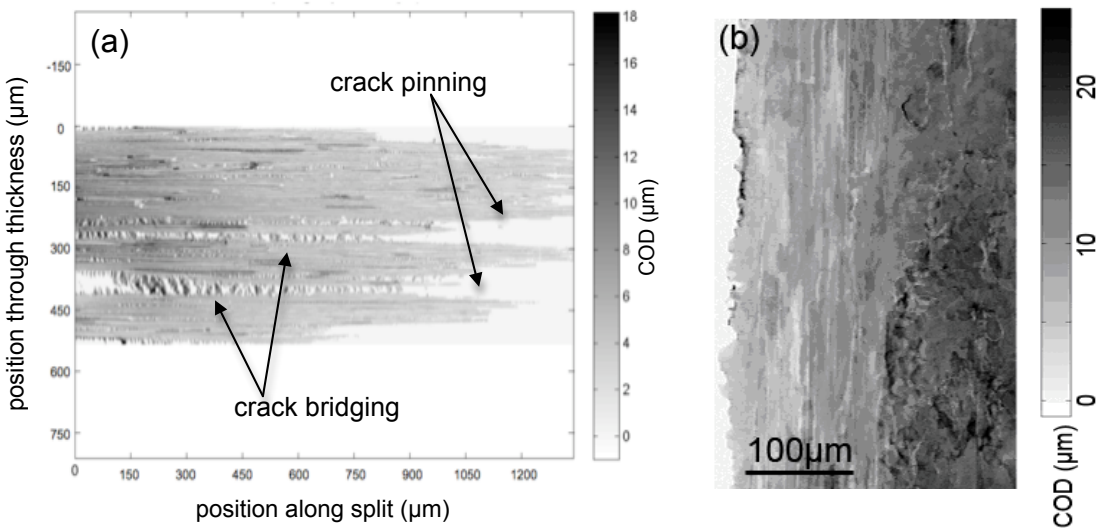

Figure 5: Grey-scale plots of crack opening displacement with position along crack. (a) 0º ply split, and (b) 90º ply transverse ply crack.

Finite Element Modeling

For the initial analysis of 0º ply splitting, elastic, 20-node quadrilateral, 3-D solid continuum elements with reduced integration points were selected. The laminate has 3 planes of geometrical symmetry to allow a model of 1/8 size to be used with appropriate boundary conditions for the nodal degrees of freedom as illustrated in Figure 6. Eight layers of elements were used to model each ply thickness. The material properties for each ply have been specified directly according to the supplier's data. The 0º and 90º ply connectivity was defined by tying together the corresponding elements of the interface surface from each ply. The crack was modelled as separated nodes that initially occupied the same co-ordinates. The overall length of the crack was in the first instance based on a straight front with area equivalence to the crack lengths observed in the SRCT images. Residual stresses induced from thermal coefficient of expansion mismatch were included in the model by simulating a constrained reduction in temperature from cure (180ºC) to room temperature.

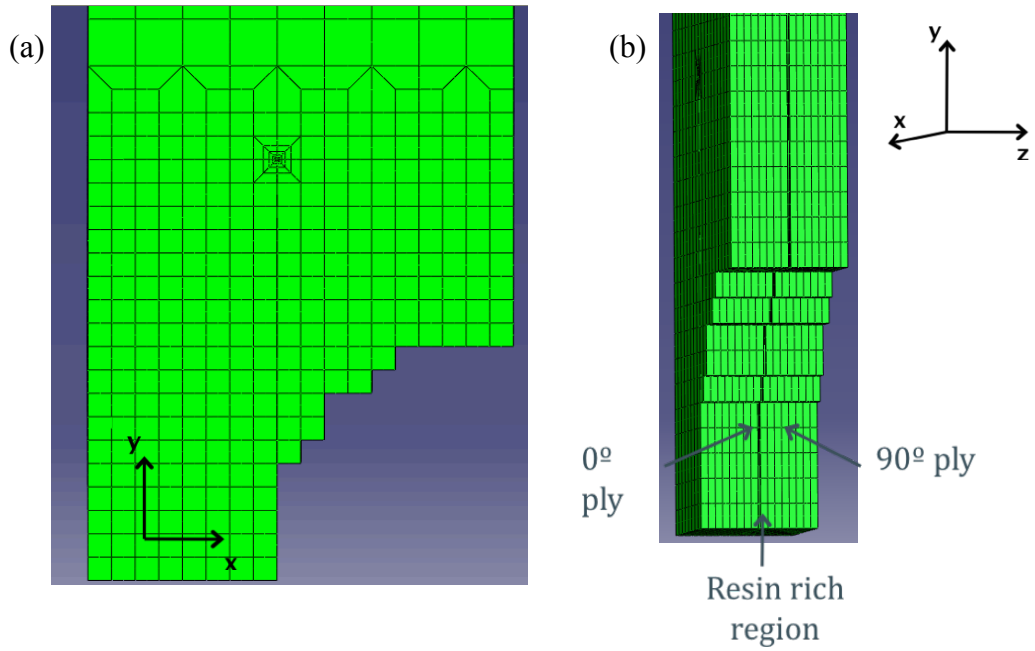

Figure 6: 3D model of 0º ply splitting. (a) Front view of 0º ply displaying crack tip and notch, and (b) side view of laminate construction.

The FE model for the TPC in a 90º ply (Figure 7) used 4-node bilinear plane stress elements with reduced integration. The mesh was locally refined in the crack tip region. Three meshes of slightly varying construction were modelled. The first and second meshes had a single resin rich region (RRR) with elastic and inelastic properties respectively, whilst the third omitted the RRR entirely. The inelastic behaviour of the rubber toughened epoxy was estimated from results of Xiao and Ye in [15].

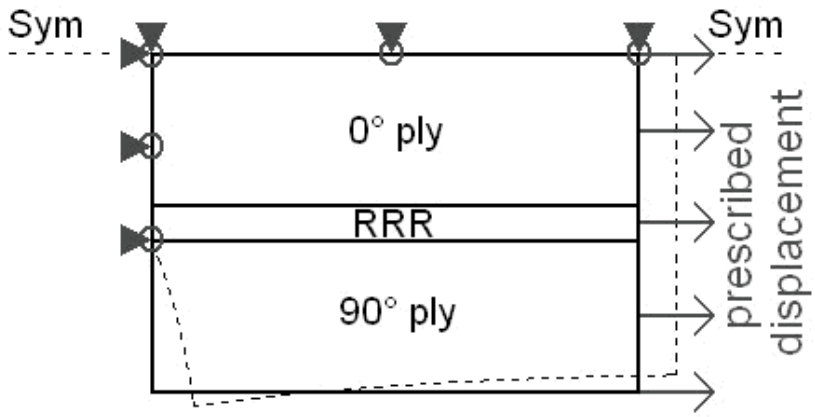

Figure 7: 2D model of a transverse ply crack with boundary conditions.

To obtain crack opening displacement, the relative movement under load along the X-axis of each node pair that represents a given split/crack was determined along the length of the crack

Experiment And Model Results Comparison

A comparison of the model results against the measured experimental results for 0º split COD in a sample loaded to 60% σ_f is shown in Figure 8. The experimental COD is plotted along the length of the crack, at four equally spaced positions through the ply thickness (1/5 being close to the 0˚/90˚ interface, 4/5 close to the centre of the laminate). Figure 8(a) shows the experimental data (averaged for the two 0˚ plies of the laminate) whilst Figure 8(b) displays the model data. The experimental data was started from the location closest to the notch at which the split was present through the entire ply thickness and was averaged over a narrow strips of the ply thickness (~10μm wide) to address partial volume segmentation effects and allow sub-voxel interpolation of opening levels (accuracy of the order of one tenth of a voxel).

Experimental data shows that, as expected, the 0º splits are most open at the root of the crack at the notch and gradually close towards the crack tip. Whilst the centre of the split (4/5 location) is most widely open, the COD otherwise appears relatively constant across the width of the ply. The COD data presented in Figure 8 shows that there is reasonable agreement between the experimental and model results: the graphs show similar trends both through the thickness of the laminate and along the length of the split, however the model predictions underestimate the crack opening displacement, particularly at locations further from the notch. Immediate limitations are evident in the comparison of an idealized model with the experimental data however, as the experimental crack clearly does not have a single simple length value to compare to the model. In addition, as identified in Figures 3, 4, and 5, there are many microstructural features that have not been accounted for in the model, most notably the bridging and crack pinning along the length of the split. There are also RRRs throughout the plies in which matrix-toughening particles have been identified. SRCT images clearly shows the resin/rubber rich region at the interface between the 0º and 90º plies. A correspondingly reduced local compliance in this region with respect to the averaged 0º lamina properties may then allow the stress gradient at the 0º/90º ply interface to act mostly across this region alone, which the model in Figure 6 does not incorporate, *i.e.* the 0˚ ply splits are unduly pinned/constrained at the ply interfaces.

Figure 9 shows the results of a comparison between the three TPC model constructions and the experimental data for transverse ply cracks in the 90º plies. As with the 0º ply splits the FE model constructs underpredict the COD to some extent, although the model with inelastic RRR can be seen to provide the closest match with the experiment COD (to within ~20% over the crack length). The trend of the experimental COD is not smooth, again highlighting the dependence of crack behaviour on local microstructure.

a)

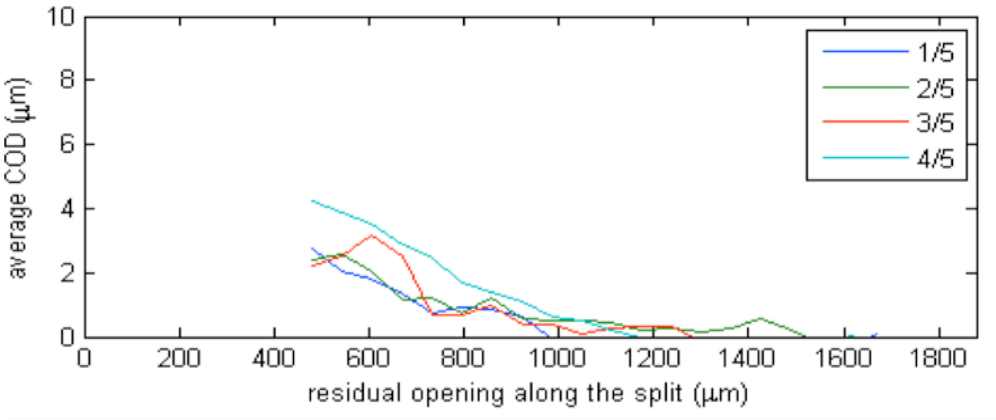

b)

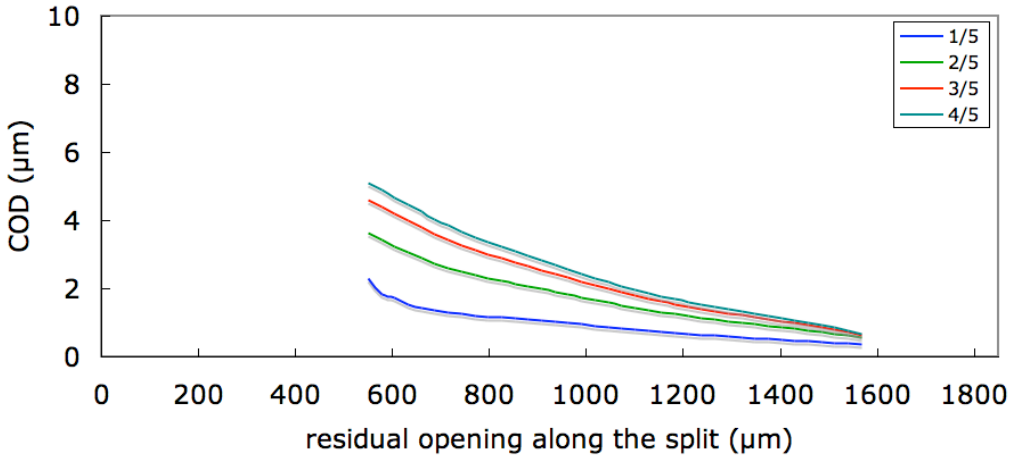

Figure 8: COD plots as a function of distance along the split for four positions through the ply thickness: (a) experiment data, and (b) model data.

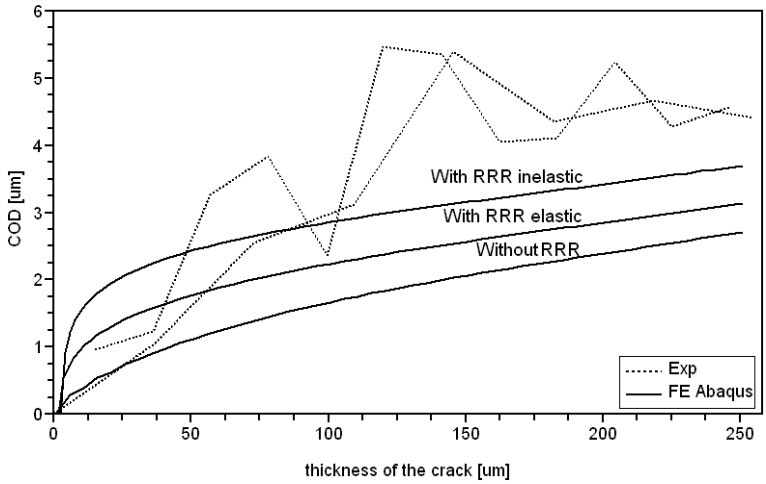

Figure 9: Comparison of FE model and experimentally measured COD.

CONCLUSIONS

SRCT observations of crack morphology have informed the development of finite element (FE) models of 0º ply splits and TPCs. The experimental data allows model predictions of COD to be evaluated with high fidelity on a scale not previously achievable in three dimensions. Such a 'data rich' approach offers a valuable tool in developing and validating future finite element simulations. Micron-scale damage can be resolved readily and full field, internal 3-D data is made available for model comparison. In general terms it is indicated that microstructural features such as RRRs at ply interfaces and crack bridging have a significant effect on matrix cracks and delaminations, with their influences being required for accurate micromechanical simulation.

ACKNOWLEDGEMENTS

The authors acknowledge: the European Synchrotron Radiation Facility (ESRF), Greg Johnson for assistance in using ESRF beamline ID19, Airbus for supplying materials and EPSRC, grant EP/E003427/1, for funding.

REFERENCES

1. Marissen, R., Westphal, T., Sterk, J.C., Fracture of quasi-isotropic composite sheets with sharp notches. *Composites Science and Technology*, 2006; 66(11-12): p. 1803-1812.
2. Kortschot, M.T. and P.W.R. Beaumont, Damage mechanics of composite materials. I. Measurements of damage and strength. *Composites Science and Technology*, 1990; 39(4): p. 289-301.
3. Barbero, E.J., G.F. Abdelal, and A. Caceres, A micromechanics approach for damage modelling of polymer matrix composites. *Composite Structures*, 2005; 67(4): p. 427-436.
2. Maimi, P., Camanho, P.P., Mayugo, J.A., Davila, C.G., A continuum damage model for composite laminates: Part I - constitutive model. *Mechanics of Materials*, 2007; 39(10): p. 897-908.
5. Iannucci, L. Ankersen, J., An energy based damage model for thin laminated composites. *Composites Science and Technology*, 2005; 66(7-8): p. 934-951.
6. Wright, P.M., Fu, X., Sinclair, I., Spearing, S.M., Ultra High Resolution Computed Tomography of Damage in Notched Carbon Fiber-Epoxy Composites. *Journal of Composite Materials*, 2008; 42(19): p. 1993-2002.
7. Ayorinde, E., Gibson, R., Kulkarni, S., Deng, F., Mahfuz, H., Islam, S., Jeelani, S., Reliable low-cost NDE of composite marine sandwich structures *Composites Part B: Engineering*. 2008; 39(1): p. 226-241.
8. Pimenta, S., Gutkin, R., Pinho, S., T. Robinson, P., A micromechanical model for kink-band formation: Part I -- Experimental study and numerical modeling. *Composites Science and Technology*, 2009; 69(7-8): p. 948-955.
9. Bussiba, A., Kupiec, M., Ifergane, S., Piat, R., Bohlke, T., Damage evolution and fracture events sequence in various composites by acoustic emission

technique. *Composites Science and Technology*, 2008; 68(5): p. 1144-1155.

10. Mizutani, Y., Nagashima, K., Takemoto, M., Ono, K., Fracture mechanism characterization of cross-ply carbon-fiber composites using acoustic emission analysis. *NDT&E International*, 1999; 33(2): p. 101 – 110.

11. Moffat, A.J., Mellor, B.G., Sinclair, I., Reed, P.A.S., The mechanisms of long fatigue crack growth behaviour in Al-Si casting alloys at room and elevated temperature. *Materials Science and Technology*, 2007; 23(12): p. 1396-1401.

12. Salvo, L., Cloetens, P., Maire, E., Zabler, S., Blandin, J.J., Buffière, J-Y, Ludwig, W., Boller, E., Bellet, D., Josserond, C., X-ray micro-tomography an attractive characterisation technique in materials science. *Nuclear Instruments and Methods in Physics Research Section B: Beam Interactions with Materials and Atoms*, 2003; 200: p. 273-286.

13. Kak, A. and M. Slaney, Principles of computerized tomographic imaging. 1988, New York, USA: IEEE press.

14. Cloetens, P., Boller, E., Ludwig, W., Baruchel, J., Schlenker, M., Absorption and phase contrast imaging with synchrotron radiation. *Europhysics News*, 2001; 32(2).

15. Xiao, K., Ye, L., Effects of rubber-rich domains and the rubber-plasticized matrix on the fracture behavior of liquid rubber-modified araldite-F epoxies. *Polymer Engineering and Science*, 2000; 40(11): p. 2288-2298.